Received: Added at production | Revised: Added at production | Accepted: Added at production

DOI: xxx/xxxx

ARTICLE TYPE

A high-order numerical method for sediment transport problems simulation and its comparison with laboratory experiments†

M.T. Capilla*[1] | A. Balaguer-Beser[2] | B. Nácher-Rodríguez[3] | F.J. Vallés-Morán[3]

[1]Departamento de Matemática Aplicada, Universitat Politècnica de València, Spain
[2]Grupo de Cartografía Geoambiental y Teledetección, Universitat Politècnica de València, Spain
[3]Instituto Universitario de Investigación de Ingeniería del Agua y Medio Ambiente, Universitat Politècnica de València, Spain

Correspondence
Email: tcapilla@mat.upv.es

Present Address
Depto. de Matemática Aplicada. Universidad Politécnica de Valencia. Camino de Vera, s/n. 46022-Valencia (Spain).

Abstract

This paper describes a high-order well-balanced central finite volume scheme for solving the coupled Exner−shallow water equations in one dimensional channels with rectangular section and variable width. Such numerical method may solve the proposed bedload sediment transport problem without the need to diagonalize the Jacobian matrix of flow. The numerical scheme uses a Runge-Kutta method with a fourth-order continuous natural extension for time discretization. The source term approximation is designed to verify the exact conservation property. Comparison of the numerical results for two accuracy tests have proved the stability and accuracy of the scheme. The results of the laboratory tests have also been used to calibrate different expressions of the solid transport discharge in the computer code. Two experimental tests have been carried out to study the erosive phenomenon and the consequent sediment transport: one test consisting of a triangular dune, and other caused by the effect of channel contraction.

KEYWORDS:
Sediment transport system; central scheme; numerical-experimental contrast

1 | INTRODUCTION

In this work a well-balanced central finite volume scheme is presented, which is fourth order accurate in time and space, for solving the coupled Shallow Water Equations (SWE)-Exner Equation system in one-dimensional channels

† A high-order numerical method for sediment transport problems.

with rectangular section and variable width. Sediment transport processes are caused by gravity effects and by friction effects with the air or the fluid containing the sediment. In this paper we focus the study on bedload sediment transport, defined as the type of transport where sediment grains roll or slide along the bed. To model the bedload sediment transport phenomenon caused by the movement of a fluid in contact with the bed sediment, we consider a coupled model constituted by a hydrodynamical component and a morphodynamical component. The hydrodynamical component is given by the Shallow Water Equations [21], used to study fluid movement in rivers, channels, etc. A sediment transport equation, depending on the bedload transport rate, is considered to model the morphodynamical component. It is necessary to develop efficient numerical methods to solve this problem accurately.

The need for high accuracy computational schemes has driven the development of numerical schemes for higher-order spatial accuracy. There have been fourth order accurate numerical methods for certain fluid flows and the convergence analysis has been establish for the incompressible Boussinesq equations [23]. Numerical methods for higher-order spatial accuracy also include weighted essentially non-oscillatory (WENO) schemes, discontinuous Galerkin (DG) schemes and $P_N P_M$ schemes (see for instance a recent review in [6]). On the other hand, the most popular numerical methods for higher-order temporal accuracy are the the Runge-Kutta methods and the ADER (Arbitrary DERivative in space and time) methods [20]. The Runge–Kutta discretization of a time-dependent ordinary differential equations splits the time evolution into a sequence of stages, each of which is only first order in time. The implementation of these methods is simple because each stage is practically identical to the previous stage. ADER schemes are computationally less expensive because the reconstruction is done only once.

Caleffi et al. [8] presented a well-balanced central weighted essentially non-oscillatory scheme, fourth-order accurate in space and in time, for numerical integration of 1D shallow water equations over movable bed. That method combines a great versatility, due to the use of the central approach, with the main advantages of the WENO schemes to achieve fourth-order formal accuracy in smooth regions while maintaining stable, to keep non-oscillatory property near strong discontinuity [24]. Even though a high order WENO schemes may use more CPU time than a second order scheme, it may still be advantageous for many application problems because of its high accuracy [19]. Balaguer and Conde [1] described a new fourth-order nonoscillatory reconstruction procedure for central schemes that satisfies shape preserving and number of extrema decreasing properties. That scheme can be an interesting computational alternative to fourth-order WENO schemes in terms of efficiency and stability. In this paper we will use central schemes with this type of spatial reconstruction.

This paper uses a central scheme to solve the proposed sediment transport problem without the need to diagonalize the Jacobian matrix of flow. This property has facilitated its application in problems by incorporating new physical parameters to the model. The numerical scheme uses a Runge-Kutta method with a fourth-order continuous natural extension for time discretization. A Gaussian quadrature rule with two integration nodes is used to evaluate the time integrals. The reconstruction operator, which calculates point values from average values, is based on a third degree polynomial that avoids increasing the number of extreme points of the solution inside each cell. Such polynomial also guarantees that the total number of local maxima and minima does not exceed the initial number of extremes and therefore prevents the development of spurious numerical oscillations. The source term approximation has been designed to verify the exact conservation property. This numerical scheme has been applied in previous works by the authors [9,2] to solve accurately other kind of problems. This paper presents its extension to solve bedload sediment transport problems in channels with a rectangular section and variable width, adding new terms of friction.

Some experimental tests in the laboratory of the Institute of Water and Environmental Engineering of the Polytechnic University of Valencia have been carried out in this paper to study the erosive phenomenon, and the consequent sediment transport. The first test case consists of a triangular dune, and the second is selected to analyze the effects of flow contraction and expansion, due to the existence of inserted structures such as bridges. Comparison of the numerical results for some accuracy tests have demonstrated the stability and accuracy of the numerical scheme and the results of the laboratory tests have been used to calibrate different expressions of the solid transport discharge

in the computer code, computing the best threshold value. The numerical results showed a good agreement with the measured experimental data.

2 | THE SEDIMENT TRANSPORT SYSTEM

The system of equations that models sediment transport in one dimensional channels with rectangular section and variable width, including the friction term, can be expressed as coupled system with the Shallow Water Equations (SWE)[22] and the Exner equation[12], given by

$$\begin{cases} h_t + (q)_x &= -q\dfrac{B'(x)}{B(x)} \\ (q)_t + \left(\dfrac{q^2}{h} + \dfrac{1}{2}gh^2\right)_x &= -gh(Z_b)_x - \dfrac{q^2}{h}\dfrac{B'(x)}{B(x)} - g\,n^2\,q\left|\dfrac{q}{h}\right| R_h^{-4/3} \\ (Z_b)_t + \xi(q_b)_x &= -\xi q_b \dfrac{B'(x)}{B(x)} \end{cases} \tag{1}$$

where $h(x,t)$ is the water depth; $q(x,t)$ is the specific discharge (flow rate per unit-width), which is related to the average horizontal velocity $v(x,t)$ by the expression $q(x,t) = h(x,t)v(x,t)$; $Z_b(x,t)$ is the bed elevation; $g = 9.8\ m/s^2$ is the acceleration of gravity; $B(x)$ is the channel width at each point; n is Manning's roughness coefficient and $R_h(x,t)$ represents the hydraulic radius, which is given by:

$$R_h(x,t) = \frac{h(x,t)B(x)}{B(x) + 2h(x,t)} \tag{2}$$

The first two equations in (1), the hydrodynamical component of the system, simulate the movement of a fluid in areas such as rivers, channels, coastal areas, etc. The third equation of the system (1), is the Exner equation and it represents the sediment transport phenomenon, defined by the solid bed flux (volume rate of transport per unit length of surface) $q_b(h,q)$, applied on the moving bed $Z_b(x,t)$. The parameter ξ is defined by:

$$\xi = \frac{1}{1-\rho_0} \tag{3}$$

where ρ_0 is the porosity of the riverbed. For the resolution of the system (1), a transport equation is necessary to evaluate q_b from the results (h,q) of the hydrodynamic module of the system. Subsequently, $Z_b(x,t)$ is obtained from the third equation of (1).

2.1 | Formulation for the bedload sediment transport rate

Bed load sediment transport can be expressed by the simple power law: $q_b(h,q) = A(q/h)^3$ as in[9], where A is a constant. However, in the comparative between numerical results and laboratory experiments to evaluate $q_b(h,q)$ in this paper, transport models were proposed for granular non-cohesive sediments[3,10]. We used well-known transport formulas based on the bed shear stress. These models, which apply for the sand size used in the experimental campaign, are the classical Meyer-Peter and Müller formulation (MPM)[15] or with Wong and Parker (W-P) correction[25], the Einstein-Brown (E-B)[11,5], Van Rijn formulation (VR)[18] and Nielsen (Niel)[17] equation. These formulations are usually expressed as a relation between three nondimensional parameters, which are the dimensionless bed-load flux q^*, the Shields stress τ^* and the dimensionless particle diameter d^*, given by

$$q^* = \frac{q_b}{\sqrt{(G-1)gd_s^3}}\,, \quad \tau^* = \frac{\tau_b}{\rho(G-1)gd_s}\,, \quad d^* = d_s\left(\frac{(G-1)g}{\nu^2}\right)^{\frac{1}{3}}\,, \tag{4}$$

where d_s is the diameter of the sediment; $G = \rho_s/\rho$ is the relative density of sediment in water and ν is the water kinematic viscosity.

Using these dimensionless parameters, sediment transport formulas used in this paper are given by

$$\text{MPM}: \quad q^* = 8(\tau^* - \tau_c^*)^{3/2}\,, \tag{5}$$

$$\text{W-P}: \quad q^* = 3.97(\tau^* - \tau_c^*)^{3/2}\,, \tag{6}$$

$$\text{VR}: \quad q^* = \frac{0.053}{d^{*0.3}}\left(\frac{\tau^*}{\tau_c^*} - 1\right)^{2.1}\,, \tag{7}$$

$$\text{Niel}: \quad q^* = 12(\tau^* - \tau_c^*)\sqrt{\tau^*}\,. \tag{8}$$

These equations assume that the movement of the granular sediment begins when the shear stress is bigger than a certain critical shear stress ($\tau^* > \tau_c^*$). This parameter can be quantified using the Shields diagram for incipient motion. The original paper of MPM [15] assumed $\tau_c^* = 0.047$ whilst W-P suggested $\tau_c^* = 0.0495$. On the other hand, Van Rijn's formulation [18] uses the following definition for τ_c^*:

$$\tau_c^* = \begin{cases} 0.24\,(d^*)^{-1} & \text{if } d^* \leq 4 \\ 0.14\,(d^*)^{-0.64} & \text{if } 4 < d^* \leq 10 \\ 0.04\,(d^*)^{-0.1} & \text{if } 10 < d^* \leq 20 \\ 0.013\,(d^*)^{0.29} & \text{if } 20 < d^* \leq 150 \\ 0.056 & \text{if } d^* > 150 \end{cases} \tag{9}$$

Instead, Einstein-Brown formulation modifies the expression of q^* depending on whether the τ^* value is less or greater than 0.182, as we see in the following definition:

$$\text{E-B}: \; q^* = \begin{cases} \frac{K\,\exp(\frac{-0.391}{\tau^*})}{0.465} & \text{if } \tau^* < 0.182 \\ 40\,K\,(\tau^*)^3 & \text{if } \tau^* \geq 0.182 \end{cases} \tag{10}$$

being:

$$K = \sqrt{\frac{2}{3} + \frac{36}{(d^*)^3}} - \sqrt{\frac{36}{(d^*)^3}}\,. \tag{11}$$

These formulas have a range of application in function of grain size and the slope of the bottom. In this work, shear stress has been obtained using Manning's coefficient given by Strickler's formula:

$$\tau^* = \frac{n^2 v^2}{(G-1)d_s R_h^{1/3}}\,,$$

where $v = v(x,t)$ is the average horizontal velocity defined below Eq. (1). To determine τ_c^* many experiments have been performed. For example, Shields proposed the well known Shields diagram. Meyer-Peter and Müller (MPM) is one of the most used models and it is applied to rivers and channels with slope lower than 2%, but the rest of the methods were subsequently introduced with the aim of trying to adjust the formulation to experimental results. In Section 4 we have used these models in order to compare numerical results with experimental data.

2.2 | Algebraic manipulation of the sediment transport system

The system of equations (1) can be rewritten using the total surface elevation, $\eta(x,t) = h(x,t) + Z_b(x,t)$, instead of the water depth $h(x,t)$, as suggested by Caleffi *et al.* in [7], resulting in this matrix form system:

$$\begin{pmatrix} \eta \\ q \\ Z_b \end{pmatrix}_t + \begin{pmatrix} q + \xi q_b \\ \frac{q^2}{\eta - Z_b} + \frac{1}{2}g(\eta - Z_b)^2 \\ \xi q_b \end{pmatrix}_x = \begin{pmatrix} -(q + \xi q_b)\dfrac{B'(x)}{B(x)} \\ -g(\eta - Z_b)(Z_b)_x - \dfrac{q^2}{\eta - Z_b}\dfrac{B'(x)}{B(x)} - g\,S_f \\ -\xi q_b \dfrac{B'(x)}{B(x)} \end{pmatrix}\,, \tag{12}$$

where S_f models the friction term by means of the Manning's law:

$$S_f = n^2\, q \left| \frac{q}{\eta - Z_b} \right| (R_h)^{-4/3}\,.$$

The matrix system (12) can be expressed as $u_t + f(u)_x = s(x,u) = s_1(x,u) + s_2(x,u) + s_3(x,u)$, where $u = u(x,t)$ is the vector of variables $u = [\eta, q, Z_b]^T$; $f(u(x,t))$ is the flux vector; $s_1(x,u)$ is the source term related to the bed slope; $s_2(x,u)$ depends on the channel width and $s_3(x,u)$ is the friction term:

$$s_1 = \begin{pmatrix} 0 \\ -g(\eta - Z_b)(Z_b)_x \\ 0 \end{pmatrix}, \quad s_2 = \begin{pmatrix} -(q + \xi q_b)\dfrac{B'(x)}{B(x)} \\ -\dfrac{q^2}{\eta - Z_b}\dfrac{B'(x)}{B(x)} \\ -\xi q_b \dfrac{B'(x)}{B(x)} \end{pmatrix}, \quad s_3 = \begin{pmatrix} 0 \\ -g\, S_f \\ 0 \end{pmatrix}. \tag{13}$$

In the next Sections we extend the methodology presented by Capilla and Balaguer in [9] to develop a high-order well-balanced numerical scheme that solves the system (12). This extension incorporates to the numerical model the new source term, $s(x, u(x,t))$, that includes the width of the channel and the friction term.

3 | NUMERICAL SCHEME

The computational domain $[0, L]$ is divided into N equally spaced nodes x_j, then the spatial step $\Delta x = L/N$ is defined. We consider 5 additional nodes on the left of $x = 0$, and also on the right of $x = L$, to avoid loss of accuracy in the domain boundaries and therefore we have the points $x_{j+\frac{1}{2}} = -5\Delta x + j\Delta x,\ j = 0, 1, \ldots, (N + 10)$. Then the nodes $x_j = \frac{1}{2}(x_{j-\frac{1}{2}} + x_{j+\frac{1}{2}}),\ j = 1, \ldots (N + 10)$ are considered.

The time interval is discretized into the values $t^0 = 0,\ t^n = t^{n-1} + \Delta t^n, n \geq 1$. The time step Δt^n is computed taking into account the following Courant-Friedrichs-Lewy or CFL condition, that is a necessary condition for the stability of numerical methods:

$$\Delta t^n = \mathrm{CFL} \frac{\Delta x}{\max\limits_j \left(\sqrt{g\hat{h}_j^n} + |\hat{v}_j^n| \right)}, \quad \mathrm{CFL} \leq 0.35 \tag{14}$$

where $\hat{h}_j^n$ and $\hat{v}_j^n$ are the point-values at time t^n of the water depth h and the water velocity v, respectively, considering $x = x_j$ when n is even and $x = x_{j+\frac{1}{2}}$ when n is odd. The use of a CFL equal to 0.45 is recommended in central schemes, when the scheme used is second order in accuracy. In river hydrodynamic models, a value between 0.30 and 0.45 is usually used to correctly represent the flow operation, without reaching prohibitive calculation times. In our case, the value of 0.35 has been a good compromise solution, thus achieving a stable model, sufficiently accurate and with acceptable computation times. This choice is related to the numerical stability of the Runge–Kutta scheme used in the time integration and the capability of this method to achieve the desired fourth order of accuracy, as can be seen in previous works with central schemes [29]. Large values of CFL number >0.35 may lead to an instable solutions.

The central scheme integrates equation (12) in the control volume $[x_j, x_{j+1}] \times [t^n, t^{n+1}]$ when n is odd, obtaining

$$\overline{u}_{j+\frac{1}{2}}^{n+1} = \overline{u}_{j+\frac{1}{2}}^{n} - \frac{1}{\Delta x}\left(\int_{t^n}^{t^{n+1}} f_{j+1}(\tau)\, d\tau - \int_{t^n}^{t^{n+1}} f_j(\tau)\, d\tau \right) + \int_{t^n}^{t^{n+1}} \overline{s}_{j+\frac{1}{2}}(\tau)\, d\tau\,, \tag{15}$$

being:

$$\overline{u}_{j+\frac{1}{2}}^{n} = \frac{1}{\triangle x} \int_{x_j}^{x_{j+1}} u(x, t^n)\, dx\,, \quad f_j(t) = f(u(x_j, t))\,, \quad \overline{s}_{j+\frac{1}{2}}(t) = \frac{1}{\triangle x} \int_{x_j}^{x_{j+1}} \sum_{k=1}^{3} s_k(x, u(x,t))\, dx\,. \tag{16}$$

At the next time step, the solution is computed on the non-staggered grid, from the calculated cell averages $\overline{u}^{n+1}_{j+\frac{1}{2}}$ and using a similar procedure:

$$\overline{u}^{n+2}_j = \overline{u}^{n+1}_j - \frac{1}{\Delta x}\left[\int_{t^{n+1}}^{t^{n+2}} f_{j+\frac{1}{2}}(\tau)\,d\tau - \int_{t^{n+1}}^{t^{n+2}} f_{j-\frac{1}{2}}(\tau)\,d\tau\right] + \int_{t^{n+1}}^{t^{n+2}} \overline{s}_j(\tau)\,d\tau\,. \tag{17}$$

The ideas described in previous works[9,16] are extended for developing the numerical scheme of this paper, considering the source term s, which also includes the channel width s_2, and the friction term s_3. As we will describe, the numerical algorithm takes into account the reconstruction, at time t^n, of averages $\overline{u}^n_{j+\frac{1}{2}}$ and point-values $\hat{u}^n_j$, and the reconstruction of Runge-Kutta fluxes, $k^{(i)}_j$. Time integration will be developed by means of a Runge-Kutta scheme coupled with a Natural Continuous Extension (NCE)[7].

In the next Subsections we describe the steps of the numerical algorithm, needed to obtain the solution (15) in a single time step.

3.1 | Reconstruction, at time t^n, of point-values and averaged values

We start the reconstruction at time $t = t^n$, with a given approximation of fourth order of the cell averages:

$$\overline{u}^n_j = \frac{1}{\Delta x}\int_{x_{j-\frac{1}{2}}}^{x_{j+\frac{1}{2}}} u\left(\varphi, t^n\right)\,d\varphi\,.$$

We analyzed[9] the definition of the reconstruction three-degree polynomial $R_j(x;\overline{u}^n)$, which approximates the pointwise values starting from the cell averages $\overline{u}^n_i$, $i \in \{j-2, j-1, j, j+1, j+2\}$, so:

$$R_j(x;\overline{u}^n) = u(x,t^n) + O((\Delta x)^4), \quad \forall x \in \left[x_{j-\frac{1}{2}}, x_{j+\frac{1}{2}}\right]\,. \tag{18}$$

We use these polynomials to approximate the point-values of the solution on the non-staggered grid at time t^n:

$$\hat{u}^n_j \equiv \overline{u}^n_j - \frac{\theta^n_j}{24}\left(\overline{u}^n_{j-1} - 2\overline{u}^n_j + \overline{u}^n_{j+1}\right)\,, \tag{19}$$

that will be used in the numerical approximation of source term and fluxes. Also, the cell-averaged values on the staggered grid at time t^n are approximated:

$$\overline{u}^n_{j+\frac{1}{2}} \equiv \frac{1}{\Delta x}\left(\int_{x_j}^{x_{j+\frac{1}{2}}} R_j(x;\overline{u}^n)\,dx + \int_{x_{j+\frac{1}{2}}}^{x_{j+1}} R_{j+1}(x;\overline{u}^n)\,dx\right)\,. \tag{20}$$

The polynomial $R_j(x,\overline{u}^n)$ has been designed in order to have the same shape as the cell-averages, $\{\overline{u}^n_{j-1}, \overline{u}^n_j, \overline{u}^n_{j+1}\}$ in the domain $I_j = \left[x_{j-\frac{1}{2}}, x_{j+\frac{1}{2}}\right]$ so that:

1. $R_j(x;\overline{u}^n)$ is monotonically increasing in I_j if $\overline{u}^n_{j-1} \le \overline{u}^n_j \le \overline{u}^n_{j+1}$.
2. $R_j(x;\overline{u}^n)$ is monotonically decreasing in I_j if $\overline{u}^n_{j-1} \ge \overline{u}^n_j \ge \overline{u}^n_{j+1}$.
3. $R_j(x;\overline{u}^n)$ has a maximum in I_j if and only if $\overline{u}^n_{j-1} < \overline{u}^n_j > \overline{u}^n_{j+1}$.
4. $R_j(x;\overline{u}^n)$ has a minimum in I_j if and only if $\overline{u}^n_{j-1} > \overline{u}^n_j < \overline{u}^n_{j+1}$.

Moreover, the parameter $\theta^{(n)}_j$ in (19) has been defined to preserve the stability and the non-oscillatory behaviour of the numerical scheme. In this way, our central approximation give rise to monotone scheme that it avoids spurious

oscillations in the solution using a fixed-central stencil. For more details see references [1,9]. To maintain the positivity of the numerical scheme we should add additional requirements to the $\theta_j^{(n)}$ definition, similar to those described by Liu and Osher [14] to satisfy the local maximum principle. This would allow a better treatment of wet/dry fronts.

In [9] a test with a dry bed generation was solved in a fixed bed suggesting that the water depth may be negative if that local maximum principle condition has not been taken into account. We could also change the definition of $\theta_j^{(n)}$ using the positivity-preserving limiter introduced by Xing et al. [28] or Xing and Shu [27]. In fact, there have been many scientific computing articles that have theoretically addressed the positivity property for certain physical variables, such as local Lax-Friedrichs type positivity-preserving flux for compressible Navier-Stokes equations [30], positivity-preserving schemes of density and pressure in ideal magnetohydrodynamics and positivity and bound-preserving limiters for the compressible Euler equations [13].

3.2 | Time integration: Runge–Kutta scheme

The time flux integrals in Eq. (15) are evaluated by means of a Gaussian quadrature rule with two integration nodes:

$$\frac{1}{\Delta x}\int_{t^n}^{t^{n+1}} f_j(\tau)d\tau \equiv \frac{\Delta t}{2\Delta x}\left(f(\hat{u}_j^{n+\beta_0}) + f(\hat{u}_j^{n+\beta_1})\right), \tag{21}$$

where $\beta_0 = 1/2\left(1 - 1/\sqrt{3}\right)$ and $\beta_1 = 1/2\left(1 + 1/\sqrt{3}\right)$. Then, we have to compute the point-values of the solution, $u(x_j, t^n + \beta_k\Delta t)$, at two intermediate time steps, $t^{n+\beta_k}$ for $k = 0, 1$. For this purpose, we apply a Runge-Kutta scheme coupled with the following Natural Continuous Extension (NCE) [4]:

$$\hat{u}_j^{n+\beta_k} \equiv u(x_j, t^n + \beta_k\Delta t) = \hat{u}_j^n + \triangle t\sum_{i=1}^{4} b_i(\beta_k)k_j^{(i)}, \tag{22}$$

where the constants $b_i(\beta_k)$ can be seen in [9] and $k_j^{(i)}, 1 \le i \le 4$ are the Runge-Kutta fluxes, which coincide with a numerical evaluation of $(-f_x + s_1 + s_2 + s_3)$ in Eq. (12) and are computed considering the point-values of $\hat{u}_k^{(i)}$, $k \in \{j-2, j-1, j, j+1, j+2\}$, being:

$$\hat{u}_j^{(1)} = \hat{u}_j^n, \quad \hat{u}_j^{(2)} = \hat{u}_j^n + \frac{\triangle t}{2}k_j^{(1)}, \quad \hat{u}_j^{(3)} = \hat{u}_j^n + \frac{\triangle t}{2}k_j^{(2)}, \quad \hat{u}_j^{(4)} = \hat{u}_j^n + \triangle t k_j^{(3)}. \tag{23}$$

3.2.1 | Reconstruction of the Runge–Kutta fluxes

We calculate the Runge-Kutta fluxes $k_j^{(i)}$, $1 \le i \le 4$ in Eq. (22), starting from the approximation described in [9]. Then we define a function given by:

$$K_j(x_k; \hat{u}^{(i)}) = -\left[f(\hat{u}_k^{(i)}) - f(\hat{u}_j^{(i)})\right] + \int_{x_j}^{x_k}\left(s_1(x, \hat{u}^{(i)}) + s_2(x, \hat{u}^{(i)}) + s_3(x, \hat{u}^{(i)})\right)dx, \tag{24}$$

where the contribution of the channel width and friction term has been incorporated into the source term of the system of equations. From the definition (24) of the function $K_j^{(i)}$, it holds that

$$\left.\frac{\partial K_j^{(i)}}{\partial x}\right|_{x=x_j} = k_j^{(i)} = (-f_x + s_1 + s_2 + s_3)_j^{(i)}. \tag{25}$$

Considering the point-values of $\hat{u}_k^{(i)}$, $k \in \{j-2, j-1, j, j+1, j+2\}$, we calculate the function $K_j(x_k; \hat{u}^{(i)})$. The integrals $\int_{x_j}^{x_k} s(x, \hat{u}^{(i)})dx$, $x_j \le x_k$ can be calculated adding integrals of the type (26), changing the sign when

$x_j > x_k$.

$$\int_{x_j}^{x_{j+1}} s(x,\hat{u}^{(i)})dx = \int_{x_j}^{x_{j+\frac{1}{2}}} P_j(x;\hat{u}^{(i)})dx + \int_{x_{j+\frac{1}{2}}}^{x_{j+1}} P_{j+1}(x;\hat{u}^{(i)})dx\,. \tag{26}$$

Using the interpolating polynomial $P_j(x;\hat{K}_j^{(i)})$ of degree three defined in[9], the evaluation of the Runge-Kutta fluxes $k_j^{(i)}$ is performed. Furthermore, in the case of a flow at rest, with $q=0$ and $\eta=$ cte, then $K_j(x_k;\hat{u}^{(i)})=0$ and this ensures that the scheme is well balanced.

3.3 | Source term integration

The time source term integrals in Eq. (15) are also evaluated using a Gaussian quadrature rule with two integration nodes:

$$\int_{t^n}^{t^{n+1}} \overline{s}_{j+\frac{1}{2}}(\tau)\,d\tau = \frac{\Delta t}{2}\left(\overline{s}_{j+\frac{1}{2}}^{n+\beta_0} + \overline{s}_{j+\frac{1}{2}}^{n+\beta_1}\right), \quad \text{with} \quad \overline{s}_{j+\frac{1}{2}}^{n+\beta_k} = \frac{1}{\triangle x}\int_{x_j}^{x_{j+1}} \sum_{i=1}^{3} s_i(x,u(x,t^n+\beta_k\triangle t))\,dx\,, \tag{27}$$

where $t^{n+\beta_k} = t^n + \beta_k\,\Delta t$ ($k=0,1$), and $\{s_i\}_{i=1}^3$ were defined in (13). The integration of the source term $s_1(u(x,\,t^{n+\beta_k}))$ in (27) is calculated using the procedure described in[9]. The first step to perform this integration consists of an integration by parts, in order to involve the spatial derivative of the free surface elevation $\eta = h + Z_b$ instead of the water depth h:

$$\begin{aligned}\overline{s}_{1,j+\frac{1}{2}}^{[2]} &= -\frac{1}{\triangle x}\int_{x_j}^{x_{j+1}} g(\eta - Z_b)\frac{\partial Z_b}{\partial x}\,dx \\ &= \frac{g}{2\triangle x}\left[\hat{Z}_{b,j+1}^2 - \hat{Z}_{b,j}^2 - 2\hat{\eta}_{j+1}\hat{Z}_{b,j+1} + 2\hat{\eta}_j\hat{Z}_{b,j}\right] + \frac{1}{\triangle x}\int_{x_j}^{x_{j+1}}\psi(x)\,dx\,,\end{aligned} \tag{28}$$

where $\psi(x) = g\,Z_b\,\frac{\partial\eta(x)}{\partial x}$. This formulation depends on the spatial derivative of the free surface level (η), which is preferable to prevent numerical errors in the solutions. In order to compute $\frac{1}{\triangle x}\int_{x_j}^{x_{j+1}}\psi(x)\,dx$ in Eq. (28), we follow this numerical treatment:

- Starting from the point-values $\hat{\eta}_j$, we compute the interpolating polynomials $P_j(x;\hat{\eta})$, that approximate the point-values $\hat{\psi}_j$ starting from point-values[9].
- We compute the polynomials $P_j(x;\hat{\psi})$ starting from the point-values $\hat{\psi}_j$ and with these polynomials, we evaluate the integration of the function $\psi(x)$ in (28).

The integrals of the source terms relative to the width channel, $s_2(u(x,t^{n+\beta_k}))$, and the friction source term $s_3(u(x,t^{n+\beta_k}))$ are evaluated using the procedure shown in (26).

4 | APPLICATIONS

In this Section, the numerical method described previously is calibrated by means of different test cases. First, in order to prove the global order of accuracy of our method, we present in Section 4.1 two accuracy tests. In Sections 4.2 and 4.3 we describe laboratory scale experiments where we simulate sediment evolution and the numerical solution is compared with the experimental data obtained by the Institute of Water and Environmental Engineering of the

Polytechnic University of Valencia. These experiments were carried out in a sand bed open channel, and they will be described in the following paragraphs.

Numerical results for these test experiments were obtained with transport equations described in Section 2.1. Different values for critical shear stress are also considered in the simulations.

These are the values considered in the comparison with laboratory experiments for the Manning coefficient n, the relative density of sediment in water G, the diameter of the sediment d_s, the porosity of the riverbed ρ_0 and the water kinematic viscosity ν:

$$n = 0.0136\,, \qquad G = \frac{\rho_s}{\rho} = 2.65\,, \qquad d_s = 0.000515\ \text{m}\,, \qquad \rho_0 = 0.4\,, \qquad \nu = 1.09 \cdot 10^{-6}\ \text{m}^2/\text{s}\,.$$

4.1 | Test 1: Accuracy tests

We tested the order accuracy of our scheme using the tests cases proposed in [26] and [8]. Initial conditions were given by the following expressions:

$$h(x,0) = 5 + e^{\cos(2\pi x)}, \quad q(x,0) = \sin\left(\cos(2\pi x)\right), \quad Z_b(x,0) = \sin^2(\pi x), \quad x \in [0,1] \tag{29}$$

and periodic boundary conditions are considered. The width of the channel was not modified at any point so $B'(x) = 0,\ \forall x \in [0,1]$ and for simplicity we assumed a null Manning's roughness coefficient so the friction term $S_f = 0$. The analytical solution is not known for this problem, and therefore we used our scheme with $NX = 12800$ cells to compute a reference solution. We took this reference solution as the exact solution in computing the numerical errors.

First, in the Exner equation we considered that $q_b(h,q) = 0$ and $\xi = 0$. It can be seen that despite the absence of sediment transport, our scheme interpolates bed elevation values on a staggered grid. Table 1 shows errors in the L^1 and L^∞ norms together with the numerical orders of accuracy, computed considering different number of cells. Final time of computation was equal to $T = 0.1$ s, when the solution is still smooth because shocks developed later in time for this problem. We can see that fourth order accuracy is achieved for this example for the free surface elevation and the specific discharge. Fig. 1 shows L^1 errors given in Table 1 versus CPU times, in a log-log scale. The points of this Figure fit a straight line.

TABLE 1 Errors at $T = 0.1$ s in L^1 and L^∞ norms and the numerical orders of accuracy considering (29) as initial conditions, periodic boundary conditions, $q_b(h,q) = 0, \xi = 0, B'(x) = 0,\ \forall x \in [0,1]$ and a null Manning's roughness coefficient.

Cells	η, free surface elevation				q, specific discharge			
	L^1	Order	L^∞	Order	L^1	Order	L^∞	Order
100	8.99E-04		1.14E-02		7.64E-03		9.11E-02	
200	7.33E-05	3.62	1.23E-03	3.20	6.15E-04	3.63	1.02E-02	3.16
400	3.95E-06	4.21	9.22E-05	3.74	3.22E-05	4.26	7.82E-04	3.71
800	1.77E-07	4.47	5.93E-06	3.96	1.35E-06	4.58	5.15E-05	3.93
1600	8.74E-09	4.34	2.62E-07	4.50	6.97E-08	4.27	2.22E-06	4.54

Second, we considered the bed load transport problem assuming that $q_b(h,q) = 0.2\left(\frac{q}{h}\right)^3$ and $\xi = \frac{1}{8}$ as in [8]. Errors in the L^1 and L^∞ norms and the numerical orders of accuracy are presented in Table 2. Shape-preserving conditions imposed to define $R_j(x,\overline{u}^n)$ may cause that the numerical scheme is not of order $O(\triangle x)^4$ in a small number of cells, so the experimental order of accuracy may be about 3 as we can see in Table 2.

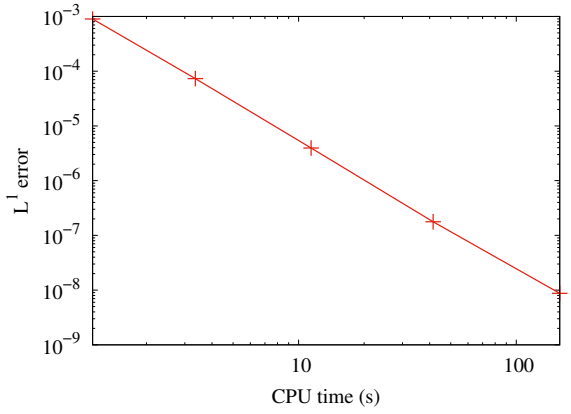

FIGURE 1 L^1 errors given in Table 1 as function of the CPU time (in seconds), in logarithmic scale.

TABLE 2 Errors in L^1 and L^∞ norms and the numerical orders of accuracy considering (29) as initial conditions, periodic boundary conditions, bed load transport with $q_b(h,q) = 0.2\left(\frac{q}{h}\right)^3$, $\xi = \frac{1}{8}$, $B'(x) = 0$, $\forall x \in [0,1]$ and a null Manning's roughness coefficient.

Cells	η, free surface elevation				q, specific discharge			
	L^1	Order	L^∞	Order	L^1	Order	L^∞	Order
200	2.96E-04		8.21E-03		2.49E-03		6.91E-02	
400	2.65E-05	3.48	1.15E-03	2.84	2.22E-04	3.49	9.69E-03	2.83
800	1.40E-06	4.25	9.53E-05	3.59	1.19E-05	4.23	8.08E-04	3.58
1600	5.94E-08	4.56	6.41E-06	3.89	5.17E-07	4.52	5.44E-05	3.89

4.2 | Test 2: Triangular dune

In the first case, we apply the numerical model presented to an experiment that consists of a triangular dune. The experimental test was developed introducing a sand layer in the laboratory channel, as it is shown in the sketch of the experiment with dimensions in Fig. 2. The dune is 0.15 m long and 0.02 m high, and it starts at x = 0.10 m and ends at x = 0.25 m. The peak is located at x = 0.215 m. The width of the channel is not modified at any point, being 0.064 m in the entire section. For the numerical computations, we consider the one-dimensional domain of 0.6 m length discretized in 360 mesh points.

As the width of the channel $B(x)$ is constant, the system of equations (12), applied to this particular test, takes this form:

$$\begin{pmatrix} \eta \\ q \\ Z_b \end{pmatrix}_t + \begin{pmatrix} q + \xi q_b \\ \dfrac{q^2}{\eta - Z_b} + \dfrac{1}{2} g(\eta - Z_b)^2 \\ \xi q_b \end{pmatrix}_x = \begin{pmatrix} 0 \\ -g(\eta - Z_b)(Z_b)_x - g\, S_f \\ 0 \end{pmatrix}. \tag{30}$$

Boundary conditions for this problem are: $q(0,t) = (8.75 \cdot 10^{-4}/0.064)$ m^2/s for the water discharge and $h(0.6,t) = 0.063$ m for the fixed downstream water depth. The following initial conditions are also considered: $h(x,0) = 0.063$ m $\forall x \in [0, 0.6]$ and $q(x,0) = (8.75 \cdot 10^{-4}/0.064)$ m^2/s $\forall x \in [0, 0.6]$. Remember that $B(x) =$

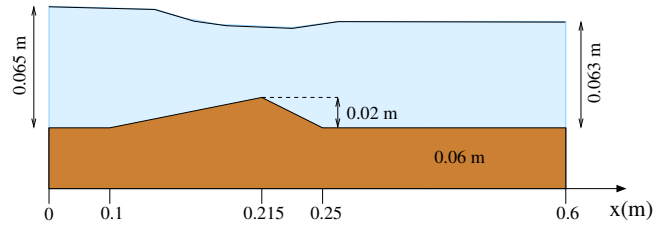

FIGURE 2 Sketch of the profile of the triangular dune case.

$0.064\ m\ \forall x$. The experimental value, $h(0,t)$ upstream, has been around 0.065 m although it will only be used for comparison.

4.2.1 | Numerical-experimental comparative for Test 2

Water surface profile

Fig. 3 shows numerical and experimental results for the free water surface at $t = 10$ min in the range 0.07 m $\leq x \leq 0.4$ m. Numerical solutions were obtained with Wong and Parker and Van Rijn models (see Eqs. (6) and (7)) considering $\tau_c^* = 0.06$; this value for τ_c^* has been chosen since the bed elevation obtained with it is closer to the experimental results as will be analyzed later in Figs. 4 and 5. The value of the critical shear stress using formula (9) is equal to 0.0311. Fig. 3 also shows the experimental result for the sand bed profile at this time step in the same range. The vertical dashed lines represent where the dune starts and ends at the initial time $t = 0$ s. Numerical water surfaces represented in Fig. 3 show that the model is able to simulate the drop in the water level that occurs when the bed level rises, under subcritical flow conditions. This same drop is observed in the experimental results, although it occurs slightly downstream.

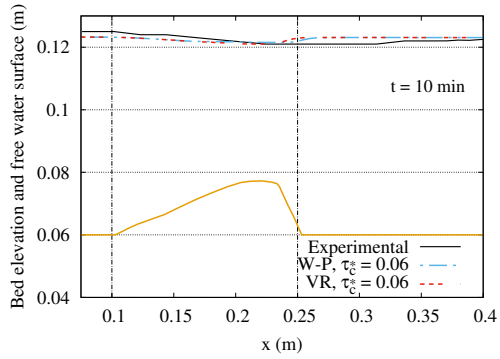

FIGURE 3 Comparison between numerical and experimental free water surface at $t = 10$ min for Test 2.

Sand bed profile

Figs. 4 and 5 show the computed profile of the dune at two time steps, t=5 min and t=10 min, together with the experimental data for this test. These Figures show numerical results obtained with the different formulations described in Section 2.1 for the bedload sediment transport rate. Classical Meyer-Peter and Müller formulation (MPM, Eq. (5)) with $\tau_c^* = 0.047$ produces excessive erosion. The same occurs with Wong and Parker (W-P) method with $\tau_c^* = 0.053$, which is the value of the dimensionless shear stress according to Shields diagram for the hydraulic conditions of the test. The results improve with this same method by increasing τ_c^* to $\tau_c^* = 0.06$, which is the maximum value that is usually recommended. The Einstein-Brown (E-B, Eq. (10)) solution is similar to that of Wong and Parker (W-P) with $\tau_c^* = 0.06$. Finally, Van Rijn's formulation (VR) using $\tau_c^* = 0.06$ produces results closer to the experimental results. This value for τ_c^* is much higher than that defined using formula (9), which would give a value equal to 0.0311.

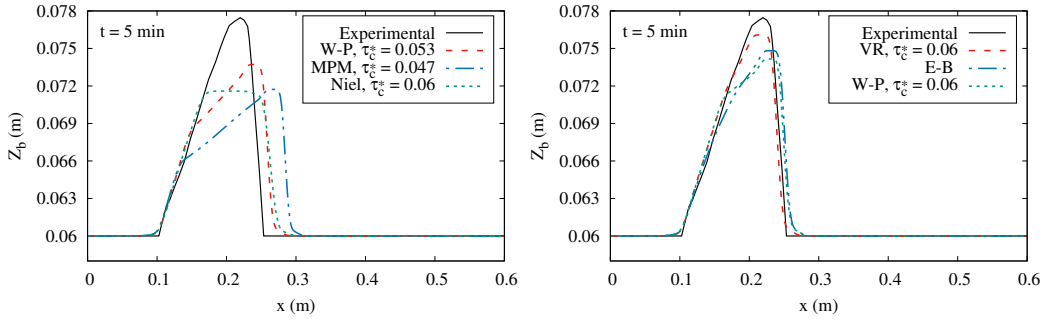

FIGURE 4 Comparison between experimental and computed sand bed profile for the triangular dune at $t = 5$ min. Left: using W-P, MPM and Nielsen models. Right: using VR, E-B and W-P models.

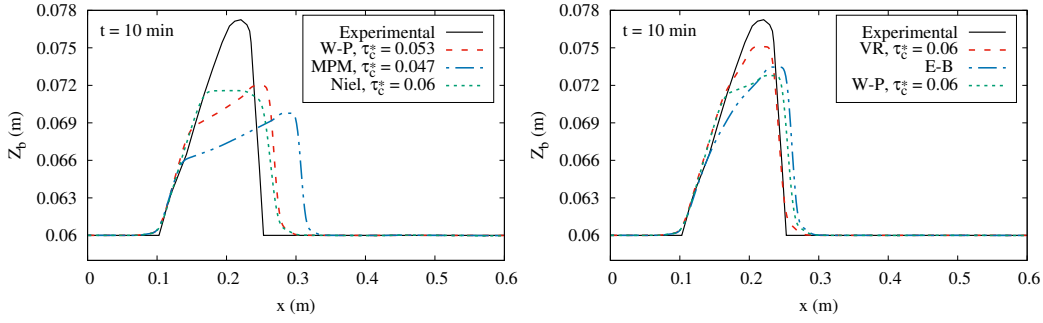

FIGURE 5 Comparison between experimental and computed sand bed profile for the triangular dune at $t = 10$ min. Left: using W-P, MPM and Nielsen models. Right: using VR, E-B and W-P models.

4.3 | Test 3: Channel with variable width

This case is selected from a set of experiments presented by Nácher-Rodríguez *et al.* in [16], to be simulated with the numerical model. Cross section of the channel is rectangular, with a variable width. The sand used to represent the river bed has a very uniform grain size distribution. The sketch and parameters for this experiment can be seen in Fig. 6. Channel length is 0.9 m with abutment plates of width 0.013 m located in the center.

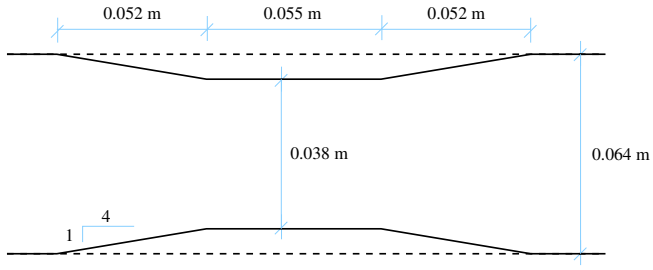

FIGURE 6 Sketch of the channel with variable width.

Simulations were carried out by establishing a constant flow rate and a fixed downstream depth as boundary conditions:

$$h(0.9,t) = 0.066 \text{ m}\,; \qquad q(0,t) = (8.8333 \cdot 10^{-4}/0.064) \text{ m}^2/\text{s}\,. \tag{31}$$

Initial conditions are the following:

$$h(x,0) = 0.066 \text{ m}\,; \qquad q(x,0) = (8.8333 \cdot 10^{-4}/0.064) \text{ m}^2/\text{s}\,; \qquad Z_b(x,0) = 0.072 \text{ m}\,. \tag{32}$$

For the numerical computations, we consider the one-dimensional domain of 0.9 m length discretized in 540 mesh points. During the test experiment, a set of photographs were made in order to analyze the profile. To extract data from pictures, two moving vertical scales were located against channel walls. Experimental results from this test comprise water surface and sand bed profiles at different time steps.

The test was carried out for a longer period of time, but after 90 min (1.5 h), we observed that the erosive part of the bed profile did not change significantly. Two different values for critical shear stress are considered in this simulation, these values are $\tau_c^* = 0.053$ and $\tau_c^* = 0.06$. As in Test 2, first value corresponds to dimensionless shear stress according to Shields diagram for the hydraulic conditions of the test. Second value was fixed in order to achieve a better agreement between numerical and experimental results.

4.3.1 | Numerical-experimental comparative for Test 3

Water surface profile

Fig. 7 shows computed versus experimental free water surface at $t = 90$ min with W-P and VR models, considering $\tau_c^* = 0.053$. With the rest of the formulations presented in Section 2.1, the changes in the free water surface are minimal and therefore, as an example, this Figure presents results with the two methods that are subsequently deeply analyzed. Fig. 7 also shows the experimental sand bed profile at $t = 90$ min along the maximum depth location; it can be seen that maximum erosion takes place close to the abutments. Vertical dashed lines represent where abutments start and where they end, and also the transitions.

We observe from that Figure that there is reasonable agreement between numerical and experimental water surfaces, despite the minor oscillations located between the abutments. These fluctuations in experimental profile located in the contracted flow area are not obtained with the numerical model.

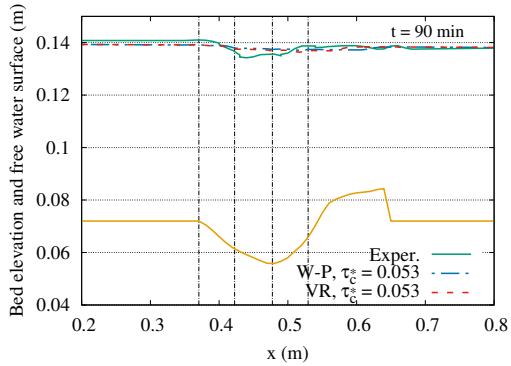

FIGURE 7 Experimental versus computed water surface profile and experimental sand bed profile, for Test 3 at t=90 min.

Sand bed profiles

Fig. 8 shows the sand bed results at time $t = 10$ min; in this Figure different transport methods are compared with each other and with the experimental data. The transport methods used in this Figure are Wong and Parker, Van Rijn, Einstein-Brown and Nielsen, with $\tau_c^* = 0.06$. We have observed that the results of this same comparison at time $t = 30$ min are very similar. In this Test, W-P and E-B methods give very similar results; in the erosion zone the W-P method is closer to the experimental result, since the maximum depth is less and therefore more similar to the experiment. From the results obtained for this Test case with the different transport models, we have selected the W-P and VR methods to carry out a more in-depth analysis, as will be shown in the following.

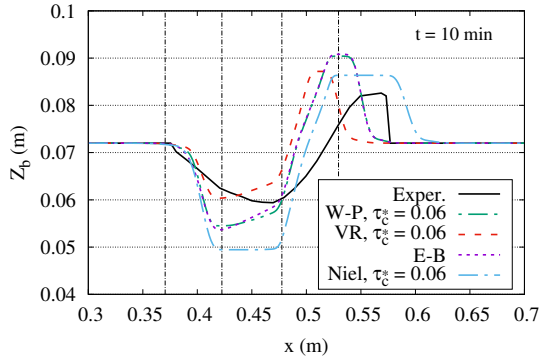

FIGURE 8 Comparison between experimental and computed sand bed profiles for Test 3 at $t = 10$ min, using different transport models.

In Fig. 9, a comparison between numerical and experimental sand bed profiles is shown for several time steps (10, 30, 60 and 90 min). Left column in the Figure shows results obtained with the W-P transport equation, and right column corresponds to VR transport equation. Results of both transport models are presented for two different values for critical shear stress ($\tau_c^* = 0.053$ and $\tau_c^* = 0.06$). It can be seen that both transport models give an erosion/deposition profile qualitatively similar to the experimental profile. Erosion is located between the abutments, and deposition starts at downstream transition. Wong and Parker formula tends to overestimate maximum scour depth, whereas Van Rijn's equation provides smaller values, more consistent with those from the experiment.

The deposition starts before in the numerical model than in the lab test. At early time steps both numerical models overestimate maximum height of deposition, but numerical and experimental tend to reach the same value after approximately 60 min. The numerical model described in this research is 1D, and it gives good results when compared to the experiment, where the flow has one main direction, which is the longitudinal one. However, the laboratory flume has a certain width (which is small, in comparison to its length) and the erosive process that takes place is intrinsically 3D, as downward and lateral flows appear as the erosion hole starts to develop. In this case, erosion is mainly caused by the increase in the longitudinal velocity of the flow due to a local narrowing of the channel, and that is why a 1D model is able to simulate the location of the scour hole and its maximum depth. However, there are other processes taking place due to the actual 3D nature of the flow, and while they are not so relevant, they play a role in the final configuration of the sand bed profile. The numerical model cannot represent that effect. Therefore, differences between the experimental and computed bed profile are to be expected.

Table 3 displays the values of the maximum scour depth and its location at different time steps; the Table compares the data of the experiment with the numerical results obtained with Wong and Parker and Van Rijn's models and considering two different values for critical shear stress. The relative errors for the values obtained for maximum depth and its location, with respect to the experimental data, are tabulated in Table 4. We can see from these Tables that solutions using Van Rijn's model with the higher Shields parameter $\tau_c^* = 0.06$, differ from experimental result by a 10%, which is acceptable taking into account the model limitations.

TABLE 3 Values of maximum scour depth and its location. Length units are in meters.

		$t = 10$ min		$t = 30$ min		$t = 60$ min		$t = 90$ min	
		Scour depth	X	Scour depth	X	Scour depth	X	Scour depth	X
Experimental		0.0126	0.469	0.0137	0.474	0.0149	0.475	0.0162	0.479
Numerical	τ_c^*								
W-P	0.053	0.0208	0.421	0.0241	0.419	0.0257	0.431	0.0261	0.441
	0.06	0.0175	0.421	0.0202	0.416	0.0211	0.444	0.0215	0.438
VR	0.053	0.0150	0.418	0.0188	0.428	0.0208	0.431	0.0216	0.436
	0.06	0.0116	0.418	0.0149	0.423	0.0167	0.433	0.0174	0.434

5 | CONCLUSIONS AND FUTURE WORK

5.1 | Conclusions

After analyzing the experimental results and the numerical comparison, we establish the conclusions of this work. We have presented a fourth order accurate central scheme that solves the 1D coupled SW–Exner Equation system in a

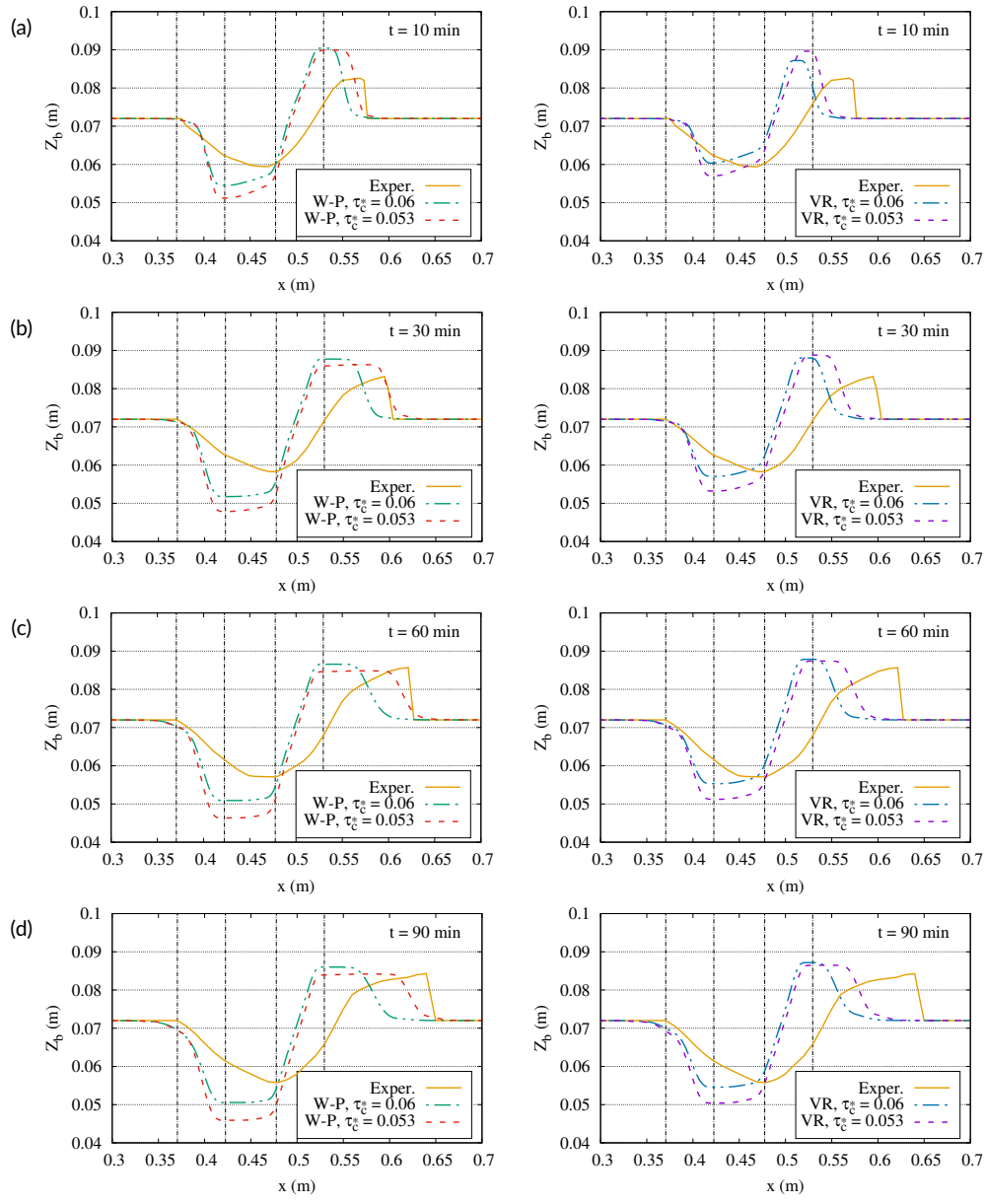

FIGURE 9 Comparison between experimental and computed sand bed profile for Test 3 at (a) $t = 10$ min, (b) $t = 30$ min, (c) $t = 60$ min and (d) $t = 90$ min. W-P model on the left, VR model on the right.

rectangular channel with variable width. The treatment for the source term spatial integration preserves the time and space accuracy and has been designed to obtain a well-balanced finite volume scheme. This central numerical scheme has been tested in previous works by the authors with other kind of problems, and now the method is extended to the incorporation of the variable width and the friction term. The method is capable of achieving great accuracy without using a very fine mesh. Its non-oscillatory behaviour prevents the presence of new outliers in the computed

TABLE 4 Relative errors in erosive profile (scour depth and location) between numerical and experimental results.

Model	τ_c^*	$t = 10$ min		$t = 30$ min		$t = 60$ min		$t = 90$ min	
		Scour depth	X	Scour depth	X	Scour depth	X	Scour depth	X
W-P	0.053	65.1	-10.3	75.9	-11.5	72.5	-9.2	61.1	-8.1
	0.06	38.9	-10.3	47.4	-12.1	41.6	-6.4	32.7	-8.7
VR	0.053	19.0	-11.0	37.2	-9.6	39.6	-9.2	33.3	-9.1
	0.06	-7.9	-11.0	8.8	-10.8	12.1	-8.8	7.4	-9.5

solutions. Also, the method allows to work with different models for the sediment transport rate and to incorporate new physical parameters in the model.

A comparative between experimental results and numerical model has been analyzed: an acceptable agreement under certain conditions was found. Figs. 4, 5, 8 and 9 show significant differences between computed sand bed profiles with different critical shear stress values. The model is highly sensitive to this parameter, and therefore special attention is required to determine its value. Model calibration is crucial in sediment transport problems, and when experimental data is not available, sensitivity analysis should always be performed to assess the model's uncertainty.

In the two laboratory tests used in this work, it was necessary to choose a higher Shields parameter τ_c^* than that used in previous references in order to obtain results closer to the experimental ones, avoiding excessive erosion. In the second laboratory test, maximum scour locating was properly computed, and the model is able to simulate both erosion and deposition, but overestimates scour depths. Then, additional modifications have to be implemented, in order to accurately compute maximum scour depths with more representative parameters.

5.2 | Future work

Transition from one to two-dimensional tests is necessary and it will provide a better representation of experimental tests. Also the incorporation in the model of a non-erodible fixed bed and the existence of bedforms, that may be the key to obtain smaller computed scour depths. Other factors have to be taken into account; for example, different bed materials and more complex structures or different angles of approach of the flow to the structure, which are factors that normally influence erosive processes.

6 | ACKNOWLEDGEMENT

This work was supported by the Generalitat Valenciana under Project AICO/2019/039. The authors thank the anonymous reviewers for their comments and suggestions.

References

1. Balaguer A. and Conde C. (2005), Fourth-order nonoscillatory upwind and central schemes for hyperbolic conservation laws. *SIAM J. Numer. Anal.* 43(2):455–473.

2. Balaguer-Beser A., Capilla M.T., Nácher-Rodríguez B., Vallés-Moran F.J. and Andrés-Doménech I. (2014). A high-order well-balanced central scheme for the shallow water equations in channels with irregular geometry. In

Advances in Differential Equations and Applications, F. Casas, V. Martinez (eds.), *SEMA SIMAI Springer Series* Vol. 4, pp 229–237, DOI 10.1007/978-3-319-06953-1.

3. Berthon C., Cordier S., Delestre O. and Le M.H. (2012). An analytical solution of the shallow water system coupled to the Exner equation. *C. R. Acad. Sci. Paris*. Ser. I 350, 183–186.

4. Bianco F., Puppo G. and Russo G. (1999), High-order central schemes for hyperbolic systems of conservation laws, *SIAM J. Sci. Comput.* 21(1):294–322.

5. Brown C.B. (1950), Sediment Transport. *Engineering Hydraulics*. Ch. 12, Rouse, H. (ed.), Wiley.

6. Busto S., Chiocchetti S., Dumbser M., Gaburro E. and Peshkov I. (2020), High order ADER schemes for continuum mechanics. *Frontiers in Physics*, 8. https://doi.org//10.3389/fphy.2020.00032

7. Caleffi V., Valiani A. and Bernini A. (2006), Fourth-order balanced source term treatment in central WENO schemes for shallow water equations. *J. Comput. Phys.* 218:228–245.

8. Caleffi V., Valiani A. and Bernini A. (2007), High-order balanced CWENO scheme for movable bed shallow water equations. *Advances in water resources.* 30(4):730–741.

9. Capilla M.T. and Balaguer-Beser A. (2012) A well-balanced high-resolution shape-preserving central scheme to solve one-dimensional sediment transport equations. *Adv. Eng. Softw.* 50:19–28.

10. Castro M.J., Fernández-Nieto E.D. and Ferreiro A.M. (2008), Sediment transport models in Shallow Water equations and numerical approach by high order finite volume methods, *Computers & Fluids.* 37(3):299–316

11. Einstein, H.A., (1942), Formulae for transportation of bed-load, Trans. ASCE, 107, 561-577.

12. Exner F. (1925), Uber die wechselwirkung zwischen wasser und geschiebe in flüssen. Sitzungsber, Akad. Wissenschaften, pt. IIa; Bd. 134.

13. Li P., Don W.S., Wang C. and Gao Z. (2018), High order positivity-and bound-preserving hybrid compact-weno finite difference scheme for the compressible Euler equations. *Journal of Scientific Computing.* 74(2):640–666.

14. Liu X.D. and Osher S. (1996), Nonoscillatory high order accurate self-similar maximum principle satisfying shock capturing schemes I. *SIAM J. Numer. Anal.* 33:760–79.

15. Meyer-Peter E. and Müller R. (1948), Formulae for bedload transport. *Proceedings of 3rd Congress, International Association of Hydraulic Research*, Sweden, 39–64.

16. Nácher-Rodríguez B., Vallés-Morán F.J., Balaguer-Beser A. and Capilla M.T. (2015), Numerical-experimental modelling of local scouring downstream of protected bridges in alluvial river beds. E-proceedings of the 36th IAHR World Congress, The Hague, the Netherlands.

17. Nielsen, P., (1992), Coastal Bottom Boundary Layers and Sediment Transport, World Scientific.

18. Van Rijn L.C. (1984), Sediment transport, part I: bed load transport, *Journal of Hydraulic Engineering.* 110(10):1431–1456.

19. Shu C.W. (2009), High order weighted essentially nonoscillatory schemes for convection dominated problems. *SIAM review.* 51(1):82–126.

20. Titarev V.A. and Toro E.F. (2002), ADER: Arbitrary High Order Godunov Approach. *Journal of Scientific Computing.* 17:609–618. https://doi.org/10.1023/A:1015126814947

21. Toro, E.F. (2001), Shock-capturing methods for free surface shallow flows, John Wiley & Sons.

22. Vázquez-Cendón, M.E. (1999), Improved treatment of source terms in upwind schemes for the shallow water equations in channels with irregular geometry, *J. Comp. Phys.* 148:497–526.

23. Wang C., Liu J.G. and Johnston H. (2004), Analysis of a fourth order finite difference method for the incompressible Boussinesq equations. *Numer. Math.* 97(3):555–594. doi: 10.1007/s00211-003-0508-3

24. Wang X., Li G., Qian S., Li J. and Wang Z. (2019), High order well-balanced finite difference WENO schemes for shallow water flows along channels with irregular geometry. *Applied Mathematics and Computation.* 363:124587.

25. Wong M. and Parker G. (2006), Reanalysis and correction of bed-load relation of Meyer-Peter and Müller using their own database. *Journal of Hydraulic Engineering.* 132(11):1159–1168.

26. Xing Y. and Shu C.W., (2005), High order finite difference WENO schemes with the exact conservation property for the shallow water equations. *Journal of Computational Physics.* 208:206–227.

27. Xing Y. and Shu C.W. (2011), High-order finite volume WENO schemes for the shallow water equations with dry states. *Advances in Water Resources.* 34(8):1026–1038.

28. Xing Y., Zhang X. and Shu C.W. (2010), Positivity-preserving high order well-balanced discontinuous Galerkin methods for the shallow water equations. *Advances in Water Resources.* 33(12):1476–1493.

29. Xu Z., Chen X.Y. and Liu Y. (2014), A new Runge-Kutta discontinuous Galerkin method with conservation constraint to improve CFL condition for solving conservation laws. *Journal of Computational Physics.* 278:348–377.

30. Zhang, X. (2017), On positivity-preserving high order discontinuous Galerkin schemes for compressible Navier-Stokes equations. *Journal of Computational Physics.* 328:301–343.